Stefan Seidel, Oliver Janka, Christopher Benndorf, Bernhard Mausolf, Frank Haarmann, Hellmut Eckert, Lukas Heletta and Rainer Pöttgen*

Ternary rhombohedral Laves phases RE_2Rh_3Ga (RE = Y, La–Nd, Sm, Gd–Er)

DOI 10.1515/znb-2016-0265
Received December 20, 2016; accepted January 24, 2017

Abstract: The ordered Laves phases RE_2Rh_3Ga (RE = Y, La–Nd, Sm, Gd–Er) were synthesized by arc-melting of the elements and subsequent annealing. The samples were characterized by powder X-ray diffraction (XRD). They crystallize with the rhombohedral Mg_2Ni_3Si type structure, space group $R\bar{3}m$. Three structures were refined from single crystal X-ray diffractometer data: a = 557.1(1), c = 1183.1(2), wR2 = 0.0591, 159 F^2 values, 10 variables for Y_2Rh_3Ga, a = 562.5(2), c = 1194.4(2) pm, $wR2$ = 0.0519, 206 F^2 values, 11 variables for Ce_2Rh_3Ga and a = 556.7(2), c = 1184.1(3) pm, $wR2$ = 0.0396, 176 F^2 values, 11 variables for Tb_2Rh_3Ga. The Rh_3Ga tetrahedra are condensed via common corners and the large cavities left by the network are filled by the rare earth atoms. The RE_2Rh_3Ga Laves phases crystallize with a *translationengleiche* subgroup of the cubic $RERh_2$ Laves phases with $MgCu_2$ type. Magnetic susceptibility measurements reveal Pauli paramagnetism for Y_2Rh_3Ga and La_2Rh_3Ga. Ce_2Rh_3Ga shows intermediate cerium valence while all other RE_2Rh_3Ga phases are Curie–Weiss paramagnets which order magnetically at low temperatures. The ^{89}Y and ^{71}Ga solid state nuclear magnetic resonance (NMR) spectra of the diamagnetic representative Y_2Rh_3Ga show well-defined single resonances in agreement with an ordered bulk phase. In comparison to the binary Laves phase YRh_2 a strongly increased ^{89}Y resonance frequency is observed owing to a higher *s*-electron spin density at the ^{89}Y nuclei as proven by density of states (DOS) calculations.

Keywords: crystal structure; intermetallics; Laves phases; magnetic properties; solid state NMR.

Dedicated to: Professor Walter Frank on the Occasion of his 60th birthday.

1 Introduction

Laves phases are an important family of AB_2 intermetallics which crystallize with three basic structure types: $MgCu_2$ (space group $Fd\bar{3}m$), $MgZn_2$ (space group $P6_3/mmc$) and $MgNi_2$ (space group $P6_3/mmc$) [1, 2]. Further stacking sequences with a different degree of hexagonality are possible [3, 4]. These phases are formed with a broad variety of element combinations. Especially the rare earth (RE)-based Laves phases RET_2 (T = 3d transition metal) [5] and TT'_2 combinations have been intensively studied with respect to their magnetic [6] and magnetocaloric properties [7], hydrogen storage [8–10] and their catalytic behavior [11]. The material properties of many of these phases were modified by substitution experiments (change of the valence electron count) on both the A and B sites, leading to a manifold of solid solutions.

Ternary Laves phases can be formed by ordered replacements of parts of the A and B atoms. The early systematic crystal chemical work by Teslyuk [12, 13] already pointed to phases of composition A_2B_3B' and $AA'B_4$ as ordering variants for $MgZn_2$ and $MgCu_2$ with the prototype phases Mg_2Cu_3Si [14] and $MgSnCu_4$ [15, 16]. Electronic and geometrical factors as well as magnetic ordering or magnetostriction play an important role for phase formation and meanwhile many different ordering variants have been reported [17–29].

An interesting case is the iron compound $TbFe_2$ [30], the first example of a direct rhombohedral distortion of the $MgCu_2$ type. Again, this distortion arises from magnetostriction. The closely related cerium compound $CeFe_2$

***Corresponding author: Rainer Pöttgen,** Institut für Anorganische und Analytische Chemie, Universität Münster, Corrensstrasse 30, 48149 Münster, Germany, e-mail: pottgen@uni-muenster.de
Stefan Seidel, Christopher Benndorf and Lukas Heletta: Institut für Anorganische und Analytische Chemie, Universität Münster, Corrensstrasse 30, 48149 Münster, Germany
Oliver Janka: Institut für Chemie, Carl von Ossietzky Universität Oldenburg, Carl-von-Ossietzky Strasse 9–11, 26129 Oldenburg, Germany
Bernhard Mausolf: Institut für Anorganische Chemie, RWTH Aachen, Landoltweg 1, 52074 Aachen, Germany
Frank Haarmann: Max-Planck-Institut für Chemische Physik fester Stoffe, Nöthnitzer Straße 40, 01187 Dresden, Germany; and Institut für Anorganische Chemie, RWTH Aachen, Landoltweg 1, 52074 Aachen, Germany
Hellmut Eckert: Institut für Physikalische Chemie, Universität Münster, Corrensstrasse 30, 48149 Münster, Germany; and Institute of Physics in Sao Carlos, University of Sao Paulo, Sao Carlos, SP 13560-590, Brazil

[31] shows the same cubic-to-rhombohedral transition under high-pressure conditions. The $TbFe_2$ type has been observed for a few Laves phases and several hydrogenated samples [32]. The symmetry reduction generates further degrees of freedom through splitting of the transition metal site and a variable c/a ratio.

The first ternary A_2B_3B' example with this rhombohedral structure was the silicide Mg_2Ni_3Si [33]. Later on, the silicides RE_2Rh_3Si (RE = Pr, Er) [34], U_2Ru_3Si [35], $Ce_2Rh_{3+x}Si_{1-x}$ [36, 37], the germanides RE_2Rh_3Ge (RE = Y, Pr, Er) [34], Ca_2Pd_3Ge [38], Sm_2Rh_3Ge [39], U_2Ru_3Ge [35], and the phosphide Mg_2Ni_3P [40] were structurally characterized.

In the present contribution we present the first gallides with $TbFe_2/Mg_2Ni_3Si$ type structures. Substitution of one fourth of the rhodium atoms in the cubic Laves phases $RERh_2$ ($\equiv RE_2Rh_4$) leads to the series of rhombohedral RE_2Rh_3Ga compounds. The synthesis, structure refinements and the magnetic properties as well as solid state nuclear magnetic resonance (NMR) spectroscopic data of these ordered Laves phases are reported herein.

2 Experimental

2.1 Synthesis

Starting materials for the synthesis of the RE_2Rh_3Ga samples were pieces of the sublimed rare earth elements (Y, La, Pr, Nd, Sm, Gd–Er from Smart Elements; Ce from Sigma Aldrich, Sigma Aldrich Germany, Hamburg), rhodium powder (Agosi, Pforzheim, Germany) and gallium lumps (Emmerich am Rhein, Germany), all with stated purities better than 99.9%. The moisture-sensitive early rare earth elements La–Nd and Sm were kept in Schlenk tubes under purified argon prior to the reactions. The argon was purified with a titanium sponge (873 K), silica gel and molecular sieves.

The elements were weighed in the ideal 2 : 3 : 1 atomic ratio (the rhodium powder was previously cold-pressed into pellets with a diameter of 5 mm) and arc-melted in a water-cooled copper mold of a MAM-1 (Edmund Bühler GmbH, Hechingen, Germany) arc-furnace under an argon atmosphere of 800 mbar. Remelting the obtained buttons several times from each site ensured complete homogeneity. With the exception of the cerium-based sample the synthesized compounds showed some impurity phases, especially in the form of non-ordered Laves phases with the presumed composition $RERh_{2-x}Ga_x$ [$MgCu_2$ type, confirmed by X-ray diffraction (XRD)].

To increase the phase purity all samples were sealed in evacuated quartz ampoules and treated with different annealing procedures. The Y_2Rh_3Ga sample was placed in the water cooled sample chamber of an induction furnace (Hüttinger Elektronik, Freiburg, Typ TIG 5/300) [41] and rapidly heated to a temperature of approximately 1100 K. This temperature was kept for 8 h until the sample was quenched by switching off the power supply of the high-frequency furnace. Also the Tb_2Rh_3Ga sample was inductively heated. A piece of the crushed arc-melted regulus was sealed in an evacuated quartz tube and heated shortly below its melting point for 10 min followed by reducing the power of the furnace within 20 min to a temperature of approximately 900 K which was kept for another 8 h followed by quenching.

The remaining samples were annealed in muffle furnaces. They were heated up to 1073 K within 2 h and then kept at this temperature for 10 (RE = La–Nd, Gd), respectively 28 days (Tb, Dy). The best results for the compounds containing holmium and erbium were obtained by annealing these samples at 773 K for 6 weeks. Except for Sm_2Rh_3Ga, these different annealing procedures led to X-ray pure samples suitable for physical property measurements. The crushed samples showed metallic luster and were stable in air over weeks.

2.2 X-ray image plate data and data collections

The RE_2Rh_3Ga bulk samples were characterized by X-ray powder diffraction using a Guinier camera equipped with an image plate system (Fujifilm, BAS-1800) using Cu Kα_1 radiation and α-quartz (a = 491.30, c = 540.46 pm) as an internal standard. The trigonal lattice parameters (Table 1) have been derived from least-squares refinements of the powder data. Comparing the experimental patterns to calculated ones [42] ensured correct indexing.

Table 1: Lattice parameters of the rhombohedral gallides RE_2Rh_3Ga, space group $R\bar{3}m$.

Compound	a (pm)	c (pm)	V (nm³)
Y_2Rh_3Ga	557.1(1)	1183.1(2)	0.3180
La_2Rh_3Ga	569.4(2)	1214.6(3)	0.3410
Ce_2Rh_3Ga	562.5(2)	1194.4(2)	0.3273
Pr_2Rh_3Ga	565.3(1)	1194.8(2)	0.3306
Nd_2Rh_3Ga	563.8(1)	1192.7(3)	0.3283
Sm_2Rh_3Ga	561.3(1)	1188.9(2)	0.3244
Gd_2Rh_3Ga	558.3(1)	1190.1(1)	0.3213
Tb_2Rh_3Ga	556.7(1)	1184.1(3)	0.3178
Dy_2Rh_3Ga	556.6(1)	1179.8(2)	0.3165
Ho_2Rh_3Ga	554.6(1)	1183.2(2)	0.3152
Er_2Rh_3Ga	552.4(1)	1180.6(3)	0.3120

As an example, we present the experimental and calculated powder pattern of Dy_2Rh_3Ga in Fig. 1.

Mechanical fragmentation of the Y_2Rh_3Ga, Ce_2Rh_3Ga and Tb_2Rh_3Ga (annealed in the induction furnace) samples resulted in irregularly shaped single crystal fragments. These were glued to thin quartz fibers using beeswax. The crystal quality was subsequently tested by Laue photographs on a Burger camera (white molybdenum radiation, image plate technique, Fujifilm, BAS-1800). The intensitiy data sets were collected at room temperature using a Stoe StadiVari single crystal diffractometer equipped with a Mo micro focus source and a Pilatus detection system.

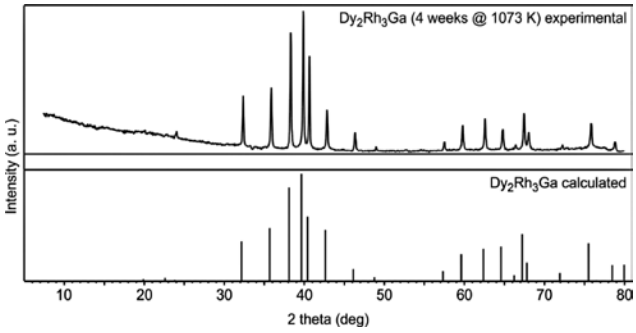

Fig. 1: Experimental (top) and calculated (bottom) Guinier powder pattern ($CuK_{\alpha 1}$ radiation) of Dy_2Rh_3Ga.

The Gaussian-shaped profile of the X-ray source required scaling along with numerical absorption corrections. All relevant crystallographic data and details of the data collections and evaluations are listed in Table 2.

2.3 EDX data

The Y_2Rh_3Ga, Ce_2Rh_3Ga and Tb_2Rh_3Ga crystals measured on the diffractometer were analyzed semi-quantitatively using a Zeiss EVO MA10 scanning electron microscope with CeO_2, TbF_3, Rh and GaP as standards. No impurity elements heavier than sodium (detection limit of the instrument) were observed. The experimentally determined element ratios (34 ± 2 at.% Y : 50 ± 2 at.% Rh : 16 ± 2 at.% Ga, 33 ± 2 at.% Ce : 52 ± 2 at.% Rh : 15 ± 2 at.% Ga and 32 ± 2 at.% Tb : 53 ± 2 at.% Rh : 15 ± 2 at.% Ga) were in close agreement with the ideal compositions (33.3 : 50 : 16.6). The variations of ± 2 at.% result from the irregular shape of the crystal surfaces (conchoidal fracture).

2.4 Physical property measurements

Fragments of the buttons of the X-ray pure phases were attached to the sample holder rod of a vibrating sample

Table 2: Crystallographic data and structure refinement for Ce_2Rh_3Ga, Tb_2Rh_3Ga and Y_2Rh_3Ga, space group $R\bar{3}m$, $Z = 3$, Mg_2Ni_3Si type.

Formula	Ce_2Rh_3Ga	Tb_2Rh_3Ga	Y_2Rh_3Ga
Molar mass, g mol^{-1}	658.7	696.3	556.2
Lattice parameters, pm	$a = 562.5(2)$	$a = 556.7(1)$	$a = 557.1(1)$
Guinier powder data	$c = 1194.4(2)$	$c = 1184.1(3)$	$c = 1183.1(2)$
Cell volume, nm^3	$V = 0.3273$	$V = 0.3178$	$V = 0.3180$
Density calc., g cm^{-3}	10.03	10.91	8.71
Crystal size, µm	20 × 30 × 60	10 × 20 × 50	10 × 20 × 50
Detector distance, mm	40	40	40
Exposure time, s	12	35	60
Integr. param. A, B, EMS	3.5; – 0.1; 0.012	7.0; – 6.0; 0.030	7.0; – 6.0; 0.030
Range in *hkl*	±9, ±9, ±19	±8, ±8, ±18	±8, ±8, ±17
$\theta_{min}/\theta_{max}$, deg	4.5/35.4	4.6/33.2	4.6/31.9
Linear absorption coeff., mm^{-1}	37.4	50.4	44.5
No. of reflections	3574	3483	3156
R_{int}	0.0761	0.0359	0.0600
No. of independent reflections	206	176	159
Reflections used [$I > 3\sigma(I)$]	187	156	127
$F(000)$, *e*	846	888	732
$R1/wR2$ for $I > 3\sigma(I)$	0.0212/0.0511	0.0173/0.0383	0.0281/0.0575
$R1/wR2$ for all data	0.0232/0.0519	0.0208/0.0396	0.0418/0.0591
Data/parameters	206/11	176/11	159/10
Goodness-of-fit on F^2	1.88	1.43	1.46
Extinction coefficient	440(30)	10(8)	–
Diff. Fourier residues (min/max), *e* Å^{-3}	– 1.61/1.31	– 1.40/0.84	– 1.20/2.02

magnetometer unit (VSM) using Kapton foil for measuring the magnetization $M(T, H)$ in a quantum design physical property measurement system (PPMS). The samples were investigated in the temperature range of 2.5–300 K with magnetic flux densities up to 80 kOe (1 kOe = 7.96×10^4 A m^{-1}). For the Nd_2Rh_3Ga and Dy_2Rh_3Ga samples additionally heat capacity (HC) measurements were conducted. A piece of the sample was fixed to a precalibrated heat capacity puck using Apiezon N grease and measured in the temperature range of 2 to 20 K.

2.5 Solid state NMR spectroscopy

The ^{89}Y and ^{71}Ga solid state NMR spectra of the diamagnetic representatives Y_2Rh_3Ga and YRh_2 were measured on Bruker DSX 500 ($B_0 = 11.7$ T), Bruker DSX 400 ($B_0 = 9.4$ T) and Bruker Avance III ($B_0 = 7.05$ T) NMR spectrometers at resonance frequencies of 24.496 MHz, 19.597 MHz (both ^{89}Y) and 91.486 MHz (^{71}Ga). The spectra were referenced to aqueous solutions of $Y(NO_3)_3$ (8 mol L^{-1} with 0.25 mol L^{-1} $Fe(NO_3)_3$; $\delta_{iso} = -22.8$ ppm) and $Ga(NO_3)_3$ (1 mol L^{-1}; $\delta_{iso} = 0$ ppm) at ambient temperature. The finely powdered sample was mixed with dry potassium chloride in an approximate volume ratio of 1 : 2 to reduce the electrical conductivity and density and was filled in conventional Si_3N_4 or ZrO_2 MAS rotors with 7 mm (Si_3N_4) and 4 mm (ZrO_2) diameter, respectively. The ^{89}Y spectra were recorded by using conventional rotor-synchronized $\pi/2$–τ–π–τ-spin-echo sequences with typical $\pi/2$-pulse lengths of 20–20.5 μs, relaxation delays of 0.5 s and MAS spinning frequencies of 4–7 kHz. Static ^{71}Ga investigations were carried out by using the wideband uniform-rate smooth truncation (WURST) QCPMG sequence [43] with the WURST-80 pulse shape and 8-step cycling version. All spectra were recorded using the Bruker Topspin software [44] and analyzed with the Dmfit software [45]. The experimental data are summarized in Table 7.

2.6 Theoretical investigations

Quantum mechanical calculation of the electric field gradient (EFG) and the density of states (DOS) for YRh_2 and Y_2Rh_3Ga were performed on the basis of density functional theory. The experimental structures were optimized with the VASP package which uses the plane augmented waves (PAW) [46] method based on the local density approximation (LDA) [47]. The cubic YRh_2 was sampled with a $14 \times 14 \times 14$ k-grid and the hexagonal Y_2Rh_3Ga with a $16 \times 16 \times 8$ k-grid. Convergence was with respect to the k-meshes and was checked carefully, and calculations were performed with a cut-off energy of 500 eV.

The full potential linear augmented plane wave (FP-LAPW) method as implemented in the WIEN2k code [48] was used to calculate the electric field gradients main principal axis V_{ZZ}(Ga) and the asymmetry parameter η_Q(Ga). The QTL and TETRA programs included in the code were applied to calculate the s-DOS of Y in both compounds. To avoid core charge leakage and to ensure that the calculations run with appropriate efficiency the atomic-sphere radii (RMT) were chosen as large as possible (Y: 2.5–2.45 a.u., Rh: 2.5–2.41 a.u. and Ga: 2.29 a.u.). The default value for the separation energies of – 6.0 Ry was chosen to separate core and valence states. The implemented GGA PBE exchange-correlation functional was chosen [49]. For the plane-wave cut-off, defined by $RMT \times K_{max}$, we applied the default value of 7. The k-meshes for WIEN2k calculations were $10 \times 10 \times 10$ for YRh_2 and the rhombohedral representation of Y_2Rh_3Ga.

3 Results and discussion

3.1 Structure refinements

Careful analyses of the three intensity data sets revealed *R*-centered lattices. The absence of further systematic extinctions led to the possible space groups $R\bar{3}m$, $R3m$, $R32$, $R\bar{3}$, and $R3$, of which the centrosymmetric group $R\bar{3}m$ was found to be correct during structure refinement. Isotypism of the RE_2Rh_3Ga compounds with the Mg_2Ni_3Si type structure [33] was already evident from the Guinier powder patterns and from a systematic check of the Pearson database [32]. Subsequently the atomic parameters of Mg_2Ni_3Si were used as starting values and the structures were refined on F^2 with anisotropic displacement parameters for all atoms using the JANA2006 [50, 51] routine. As a check for the correct composition and site assignment, the occupancy parameters were refined in a separate series of least-squares cycles. All sites were fully occupied within three standard deviations. No significant residual peaks were evident in the final difference Fourier syntheses. At the end, the positional parameters were transformed to the setting required for the group–subgroup scheme discussed below. The final positional parameters and interatomic distances are listed in Tables 3–5.

Further details of the structure refinements may be obtained from FIZ Karlsruhe, 76344 Eggenstein-Leopoldshafen, Germany (fax: +49-7247-808-666; e-mail:

Table 3: Atom positions and equivalent isotropic displacement parameters (pm²) for Ce_2Rh_3Ga, Tb_2Rh_3Ga and Y_2Rh_3Ga.

Atom	Wyckoff position	x	y	z	U_{eq}
Ce_2Rh_3Ga					
Ce	6*c*	0	0	0.37198(5)	171(2)
Rh	9*d*	1/2	0	1/2	148(2)
Ga	3*a*	0	0	0	134(3)
Tb_2Rh_3Ga					
Tb	6*c*	0	0	0.37090(4)	144(2)
Rh	9*d*	1/2	0	1/2	127(2)
Ga	3*a*	0	0	0	109(3)
Y_2Rh_3Ga					
Y	6*c*	0	0	0.36984(16)	179(4)
Rh	9*d*	1/2	0	1/2	155(3)
Ga	3*a*	0	0	0	144(6)

U_{eq} is defined as one third of the trace of the orthogonalized U_{ij} tensor.

Table 4: Anisotropic displacement parameters (pm²) for Ce_2Rh_3Ga, Tb_2Rh_3Ga and Y_2Rh_3Ga.

Atom	U_{11}	U_{22}	U_{33}	U_{12}	U_{13}	U_{23}
Ce_2Rh_3Ga						
Ce	162(2)	U_{11}	189(3)	81(1)	0	U_{13}
Rh	151(2)	124(3)	159(3)	62(1)	7(1)	15(2)
Ga	142(4)	U_{11}	120(5)	71(2)	0	U_{13}
Tb_2Rh_3Ga						
Tb	138(2)	U_{11}	157(2)	69(1)	0	U_{13}
Rh	126(2)	99(3)	146(3)	50(1)	7(1)	13(2)
Ga	116(4)	U_{11}	95(5)	58(2)	0	U_{13}
Y_2Rh_3Ga						
Y	172(5)	U_{11}	193(8)	86(2)	0	U_{13}
Rh	161(4)	128(5)	166(4)	64(2)	5(2)	10(4)
Ga	150(7)	U_{11}	132(11)	75(4)	0	U_{13}

Coefficients U_{ij} of the anisotropic displacement factor tensor of the atoms are defined by: $-2\pi^2[(ha^*)^2U_{11}+\ldots+2hka^*b^*U_{12}]$.

Table 5: Interatomic distances (pm) for Ce_2Rh_3Ga, Tb_2Rh_3Ga and Y_2Rh_3Ga. All distances of the first coordination spheres are listed.

Ce_2Rh_3Ga				Tb_2Rh_3Ga				Y_2Rh_3Ga			
Ce:	3	Rh	294.1	Tb:	3	Rh	290.4	Y:	3	Rh	289.2
	1	Ce	305.8		1	Tb	305.7		1	Y	308.0
	6	Rh	320.1		6	Rh	317.6		6	Rh	318.3
	3	Ga	328.0		3	Ga	324.5		3	Ga	324.5
	3	Ce	337.6		3	Tb	333.5		3	Tb	333.0
Rh:	2	Ga	256.9	Rh:	2	Ga	254.5	Rh:	2	Ga	254.4
	4	Rh	281.3		4	Rh	278.3		4	Rh	278.6
	2	Ce	294.1		2	Tb	290.4		2	Y	289.2
	4	Ce	320.1		4	Tb	317.6		4	Y	318.3
Ga:	6	Rh	256.9	Ga:	6	Rh	254.5	Ga:	6	Rh	254.4
	6	Ce	328.0		6	Tb	324.5		6	Y	324.5

All standard uncertainties were less than 0.2 pm.

crysdata@fiz-karlsruhe.de) on quoting the deposition numbers CSD-432339 (Y_2Rh_3Ga), CSD-432341 (Ce_2Rh_3Ga) and CSD-432340 (Tb_2Rh_3Ga).

3.2 Crystal chemistry

The gallides RE_2Rh_3Ga (*RE* = Y, La–Nd, Sm, Gd–Er) are new representatives of the Mg_2Ni_3Si type structure [33], space group $R\bar{3}m$, Pearson symbol *hR*18 and Wyckoff sequence *dca*. The cell volumes (Table 1 and Fig. 2) decrease from the lanthanum to the erbium compound as expected from the lanthanide contraction. Ce_2Rh_3Ga shows a drastic deviation from this smooth behavior. The significantly smaller cell volume (even smaller than Nd_2Rh_3Ga) is a clear hint for an intermediate cerium valence. This is discussed in more detail below along with the magnetic properties. A very similar trend of the cell volume is observed for the cubic Laves phases $RERh_2$ (Fig. 2) [32]. The cell volumes per formula unit (*Z*) of the gallides are slightly larger than those of the $RERh_2$ phases. This trend is also observed in the sequence $GdRh_2$ ($MgCu_2$ type, $V/Z = 0.0530$ nm³ [52]) → GdRhGa (TiNiSi type, $V/Z = 0.0573$ nm³ [53]) → $GdGa_2$ (AlB_2 type, $V/Z = 0.0639$ nm³ [54]), indicating generally stronger *RE*–Rh vs. weaker *RE*–Ga bonding. Small anomalies in the *c* lattice parameter of the RE_2Rh_3Ga samples might be indicative of small homogeneity ranges.

The crystal structure of Ce_2Rh_3Ga is exemplarily presented in Fig. 3 and discussed in the following. The network of condensed tetrahedra shows full rhodium-gallium ordering. All Rh_3Ga tetrahedra exclusively share corners, but in a well-defined motif. The Kagomé networks which extend in the *ab* plane are formed only by the rhodium atoms, and the gallium atoms connect adjacent networks. This ordering pattern leads to substantial differences in the geometry of the tetrahedra. Each rhodium atom has two gallium neighbors at 257 pm and four rhodium neighbors at the much longer distance of 281 pm.

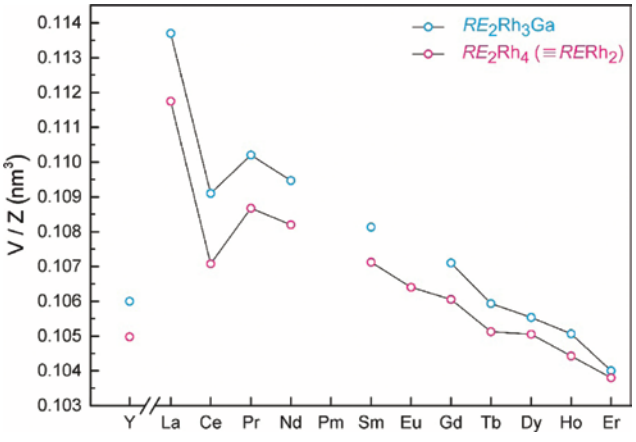

Fig. 2: Plot of the cell volumes of the RE_2Rh_3Ga and $RERh_2$ [32] Laves phases as a function of the rare earth element.

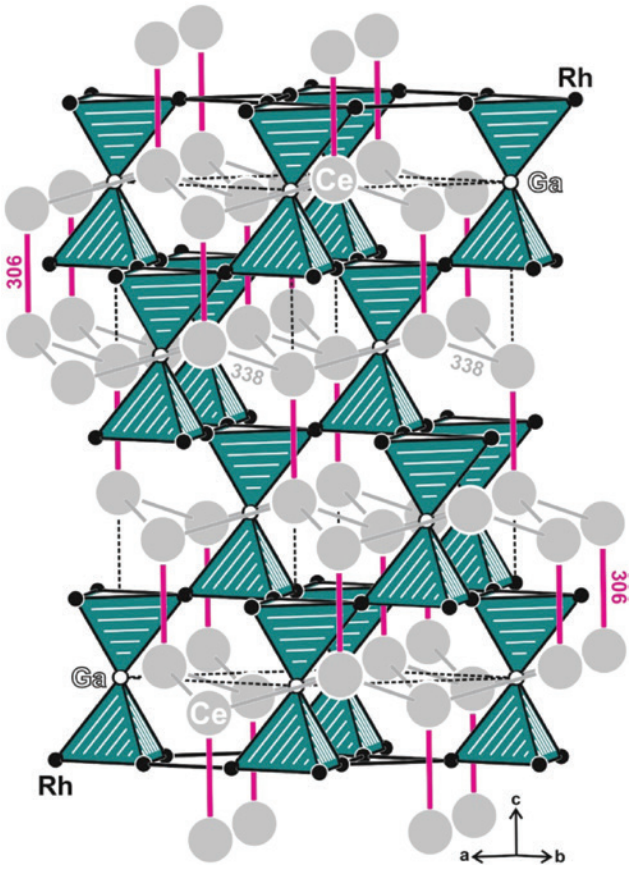

Fig. 3: The crystal structure of Ce_2Rh_3Ga. Cerium, rhodium, and gallium atoms are drawn as medium gray, black filled and open circles, respectively. The network of condensed Rh_3Ga tetrahedra and the diamond-related cerium substructure (magenta lines for the shorter and gray lines for the longer Ce–Ce distances) are emphasized. Interatomic distances are given in pm.

The Rh–Ga distance of 257 pm is indicative of substantial Rh–Ga bonding. It is only slightly longer than the sum of the covalent radii for Rh + Ga of 250 pm [55]. The [RhGa] (265–268 pm Rh–Ga) and [Rh_3Ga_9] (259–263 pm Rh–Ga) networks of CeRhGa [56] and $Eu_2Rh_3Ga_9$ [57] show even longer Rh–Ga distances.

The cerium atoms fill the large cavities formed by the network of tetrahedra. The topology reminds of the diamond structure. The substantial Rh–Ga interlayer bonding (between the Kagomé networks) leads to a strong decrease of the c/a ratio ($\sqrt{2}\sqrt{3} = 2.45$ for $CeRh_2$ [52] in a related setting vs. 2.12 for Ce_2Rh_3Ga) and this directly influences the Ce–Ce distances: 4×327 pm in $CeRh_2$ *vs.* 1×306 and 3×338 pm in Ce_2Rh_3Ga. All of these Ce–Ce distances are well below the Hill limit [58] for *f* electron localization (340 pm). This is in full agreement with the intermediate cerium valence (*vide infra*) and the absence of any magnetic ordering.

The structures of $CeRh_2$ ($\equiv Ce_2Rh_4$) and Ce_2Rh_3Ga are strictly related by a group–subgroup scheme, which is presented in the Bärnighausen formalism [59–61] in Fig. 4. The *translationengleiche* symmetry reduction of index 4 (t4) from $Fd\bar{3}m$ to $R\bar{3}m$ leads to a splitting of the 16*c* rhodium site, enabling the 3 : 1 Rh/Ga ordering. Furthermore, we obtain a free c/a ratio and a free z parameter for the cerium atoms. These parameters allow the optimization of chemical bonding forced by the rhodium/gallium coloring. A 7 : 1 ordering on the tetrahedral network has recently been reported for orthorhombic Cd_4Cu_7As [28].

Finally we focus on the valence electron count (VEC) of $RERh_2$ and RE_2Rh_3Ga ($\equiv RERh_{1.5}Ga_{0.5}$). The formation of a cubic or a hexagonal Laves phase depends on VEC. Johnston and Hoffmann [62] calculated the variation of the relative energy of the hexagonal and cubic tetrahedral network of Laves phases as a function of VEC. Cubic $RERh_2$ (VEC = 21) and hexagonal $RERh_{1.5}Ga_{0.5}$ (VEC = 18) perfectly match the predictions. Even the two cerium compounds with slightly higher VEC (a consequence of intermediate cerium valence; *vide infra*) fall in the same range.

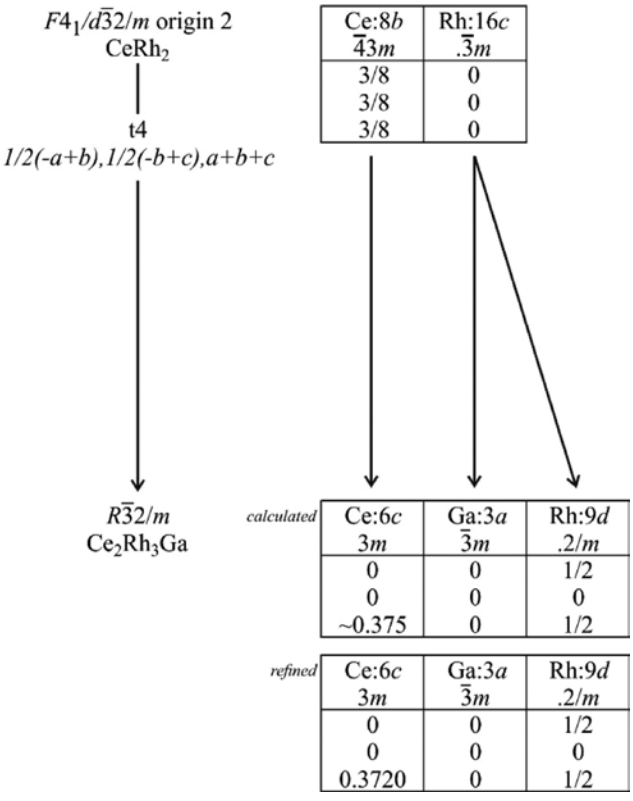

Fig. 4: Group–subgroup scheme in the Bärnighausen formalism [59–62] for the structures of $CeRh_2$ [52] and Ce_2Rh_3Ga. The index for the *translationengleiche* (t) symmetry reduction, the unit cell transformation, and the evolution of the atomic parameters are given.

Table 6: Magnetic properties of the gallides RE_2Rh_3Ga.

	T_N (K)	T_C (K)	μ_{eff} (μ_B)	μ_{calc} (μ_B)	θ_p (K)	H_{crit} (kOe)	μ_{sat} (μ_B)	$g_J \times J$ (μ_B)
Pr_2Rh_3Ga	–	6.3(1)	3.54(1)	3.58	3.8(1)	–	1.6(1)	3.20
Nd_2Rh_3Ga	–	4.8(1)	3.58(1)	3.62	6.4(1)	–	1.7(1)	3.27
Gd_2Rh_3Ga	43.0(1)	–	8.03(1)	7.94	51.7(1)	6.69(5)	7.0(1)	7
Tb_2Rh_3Ga	33.4(1)	–	9.47(1)	9.72	37.5(1)	4.49(5)	7.0(1)	9
Dy_2Rh_3Ga	–	10.9(1)	11.01(1)	10.65	11.7(1)	–	8.7(1)	10
Ho_2Rh_3Ga	–	10.9(1)	10.56(1)	10.61	20.9(1)	–	8.3(1)	10
Er_2Rh_3Ga	–	13.1(1)	9.70(1)	9.58	5.0(1)	–	5.1(1)	9

T_N, Néel temperature; T_C, Curie temperature; μ_{eff}, effective magnetic moment; μ_{calc}, calculated magnetic moment; θ_p, paramagnetic Curie temperature; H_{crit}, critical field for the spin reorientation, saturation moment; μ_{sat} and saturation according to $g_J \times J$. The experimental saturation magnetizations were obtained at 3 K and 80 kOe.

3.3 Magnetic properties

Magnetic susceptibility data has been obtained only for the X-ray pure RE_2Rh_3Ga samples with RE = Y, La–Nd, and Gd–Er. The basic magnetic data that has been derived from these measurements are listed in Table 6. The results are discussed in the following paragraphs.

3.3.1 Y_2Rh_3Ga and La_2Rh_3Ga

The temperature dependences of the magnetic susceptibility of the yttrium and lanthanum compound are presented in Fig. 5. Both compounds are Pauli paramagnets with room temperature susceptibilities of $\chi = 1.85(1) \times 10^{-4}$ emu mol^{-1} and $\chi = 1.30(1) \times 10^{-3}$ emu mol^{-1}, respectively. The weak upturns at lower temperature arise from tiny amounts of paramagnetic impurities. The present data clearly proves the absence of local moments on the rhodium atoms. Thus, the magnetic properties of the remaining phases arise from the rare earth elements only.

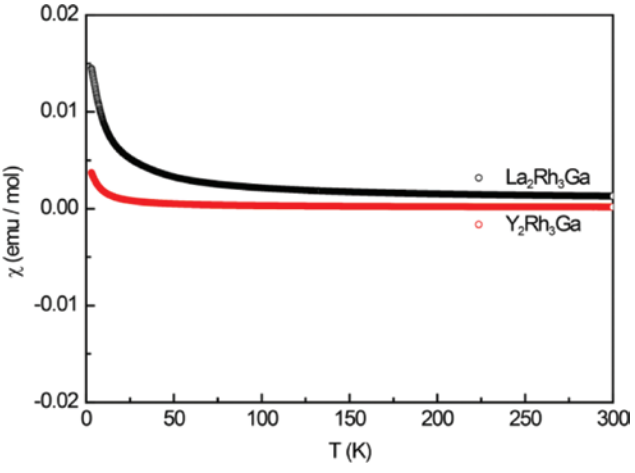

Fig. 5: Temperature dependence of the magnetic susceptibility (χ data) of Y_2Rh_3Ga (red) and La_2Rh_3Ga (black) measured at 10 kOe.

3.3.2 Ce_2Rh_3Ga

The susceptibility and inverse susceptibility data of Ce_2Rh_3Ga are shown in Fig. 6 (top), indicating values in the order of 10^{-3} emu mol^{-1} without any sign of magnetic ordering down to low temperatures. The χ^{-1} data is curved, consequently no Curie–Weiss behavior is observed. The shape of the χ^{-1} curves with the weak temperature dependence is typical for Ce-based intermetallics which exhibit valence fluctuations. The magnetic susceptibility of valence fluctuating compounds can be described with the so called interconfiguration fluctuation (ICF) model proposed by Hirst [63], which was later applied by Sales and Wohlleben in order to explain valence fluctuation behavior in intermetallic Yb compounds [64]. The ICF model can be used for systems were two distinct states of the rare earth atom, here Ce^{3+} and Ce^{4+}, exist. The temperature dependence of the magnetic susceptibility is described as:

$$\chi(T) = \left(\frac{N_A}{3k_B}\right)\left[\frac{\mu_n^2 \nu(T) + \mu_{n-1}^2\{1-\nu(T)\}}{T+T_{sf}}\right] + n\frac{C}{T} + \chi_0 \qquad (1)$$

with N_A being the Avogardo's number, k_B the Boltzmann constant, μ the magnetic moment of the respective Ce ion and the spin fluctuation temperature T_{sf}. χ_0 is a temperature independent term, C the Curie constant (for free Ce^{3+}, $C = 0.807$ emu mol^{-1} K^{-1}), and n the fraction of stable Ce^{3+}. The overall susceptibility is described by three terms: (i) a valence fluctuation part, (ii) the contribution of the stable Ce^{3+} ions and (iii) a temperature independent part. The valence fluctuations are described by the pseudo-Boltzmann statistic shown in equation (2) which contains the spin fluctuation temperature T_{sf} and E_{ex} describing the

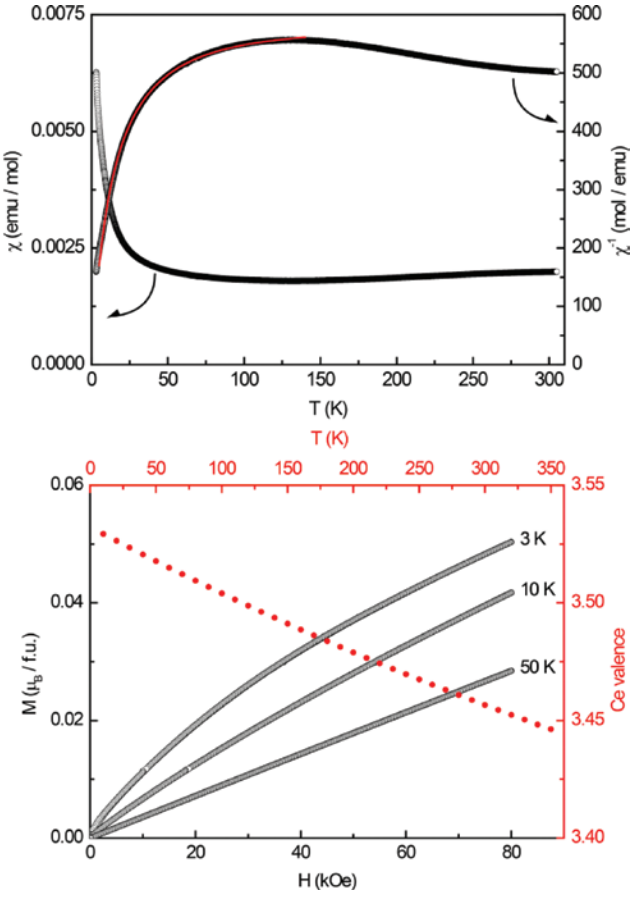

Fig. 6: Magnetic properties of Ce_2Rh_3Ga. Top: temperature dependence of the magnetic susceptibility (χ and χ^{-1} data) measured at 10 kOe; the fit according to Sales and Wohlleben is depicted in red. Bottom: Magnetization isotherms at 3, 10, and 50 K along with the calculated temperature dependence of the cerium valence, depicted in red.

energy difference between the two cerium ground states according to $E_{ex} = E(Ce^{3+}) - E(Ce^{4+})$.

$$\nu(T) = \frac{(2J_n + 1)}{\left\{(2J_n + 1) + (2J_{n-1} + 1)\exp\left[-\frac{E_{ex}}{k_B(T + T_{sf})}\right]\right\}} \quad (2)$$

For the Ce cations the fluctuations take place between the $4f^0$ and $4f^1$ configurations. With $J_1 = \mu_{eff,1} = 0$, $J_2 = 5/2$ and $\mu_{eff,2} = 2.54\ \mu_B$ the magnetic data can be fitted and $T_{sf} = 1599(15)$ K, $E_{ex} = 3072(27)$ K, $n = 0.0268$ and $\chi_0 = 1.6 \times 10^{-3}$ emu mol^{-1} were extracted. In order to prevent over-determination, the temperature independent part χ_0 and n were fitted first and fixed for the rest of the procedure, hence no standard deviations are given for these two parameters. The extracted values for T_{sf} and E_{ex} are larger compared to, e.g. valence fluctuating $CeMo_2Si_2C$ [65], $CeRhSi_2$ [66] or $Ce_2Rh_3Si_5$ [66], but comparable to the ones found for the solid solutions $CeRu_{1-x}Ni_xAl$ [67] or $CeRu_{1-x}Pd_xAl$ [68]. In addition to parameters extracted from the fitted data, the average cerium valence can be obtained using eq. 2 to calculate ν(T). The change of the cerium valence vs. temperature is plotted in Fig. 6 (bottom, red), showing a temperature-dependent shift of the cerium valence. The magnetization isotherms exhibit highly reduced magnetic moments with saturation magnetizations of $\mu_{sat} = 0.05(1)$ μ_B per formula unit compared to the expected magnetization of $\mu_{sat,theo} = 2.14$ according to $g_J \times J$.

Finally it is interesting to note that binary $CeRh_2$ also shows intermediate cerium valence. This was substantiated for polycrystalline material as well as for Czochralski grown single crystals via resistivity measurements, evaluation of the de Haas–van Alphen effect and L_{III} absorption studies [69, 70].

3.3.3 Pr_2Rh_3Ga–Er_2Rh_3Ga

For the remaining RE_2Rh_3Ga series with RE = Pr, Nd, and Gd–Er conventional magnetism with cooperative ordering phenomena is observed. The magnetic measurements are depicted in Figs. 7–13. The top panels show the magnetic susceptibility (χ and χ^{-1} data), measured at 10 kOe. The paramagnetic region is fitted using the Curie-Weiss law to extract the effective magnetic moment μ_{eff} and the Weiss constant θ_P (listed in Table 6). For all compounds the effective magnetic moments are in good agreement with the calculated theoretical moments μ_{calc}. The middle panels depict the zero-field cooling (ZFC) and field-cooling (FC) measurements at an external field of 100 Oe. The bottom panels display the magnetization isotherms recorded at different temperatures. The isotherms way above the ordering temperatures show linear temperature dependencies, as expected for paramagnetic materials. The saturation magnetization (μ_{sat}) was determined from the 3 K isotherm at 80 kOe. In the following paragraphs the measurements of the individual compounds are briefly discussed and interesting features are outlined.

The ZFC/FC measurements of Pr_2Rh_3Ga (Fig. 7) show an anomaly characteristic for ferromagnetic ordering at $T_C = 6.3(1)$ K. The transition temperature was determined from the derivative $d\chi/dT$ vs. T curve (Fig. 7, middle, inset). The magnetization isotherm recorded at 3 K confirms the ferromagnetic ground state of Pr_2Rh_3Ga.

Two anomalies occur in the ZFC/FC measurements of Nd_2Rh_3Ga (Fig. 8). This is unusual since the crystal structure contains only one rare earth site, therefore additional heat capacity measurements were conducted (Fig. 8, middle, red). One observes a sharp λ-shaped

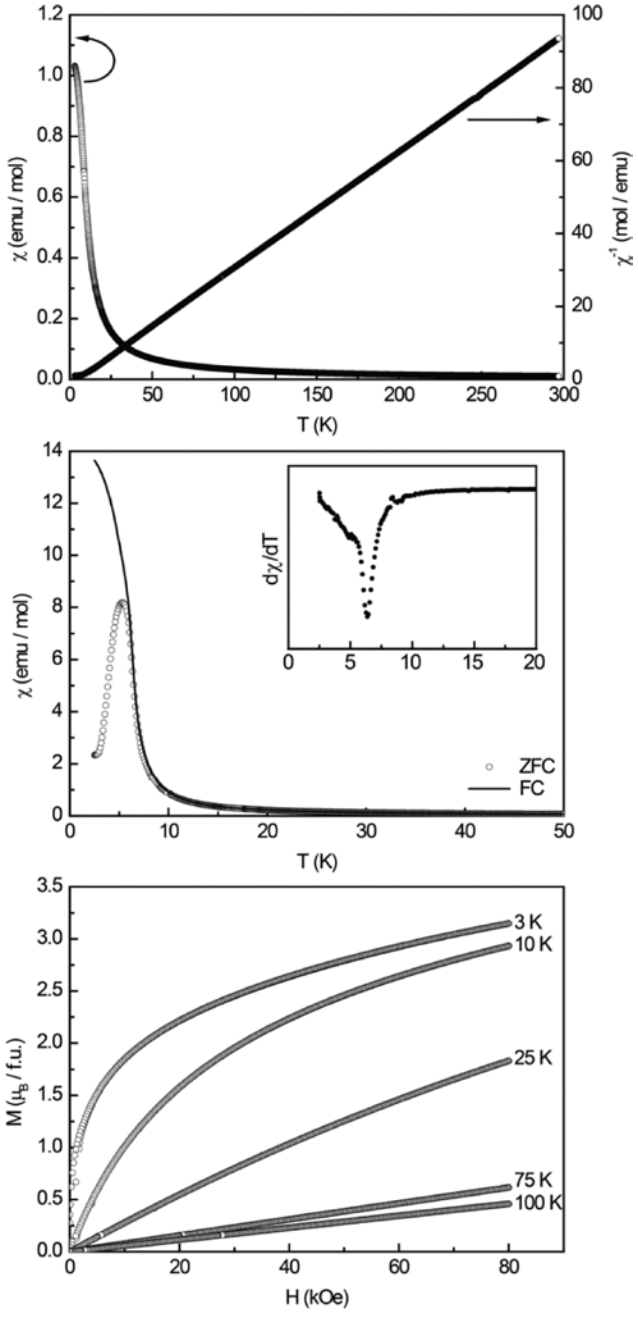

Fig. 7: Magnetic properties of Pr_2Rh_3Ga. Top: temperature dependence of the magnetic susceptibility (χ and χ^{-1} data) measured at 10 kOe. Middle: temperature dependence of the magnetic susceptibility in zero-field cooling and field cooling mode measured at 100 Oe; the inset shows the derivative $d\chi/dT$ vs. T used to determine the Curie-temperature. Bottom: Magnetization isotherms at 3, 10, 25, 75, and 100 K.

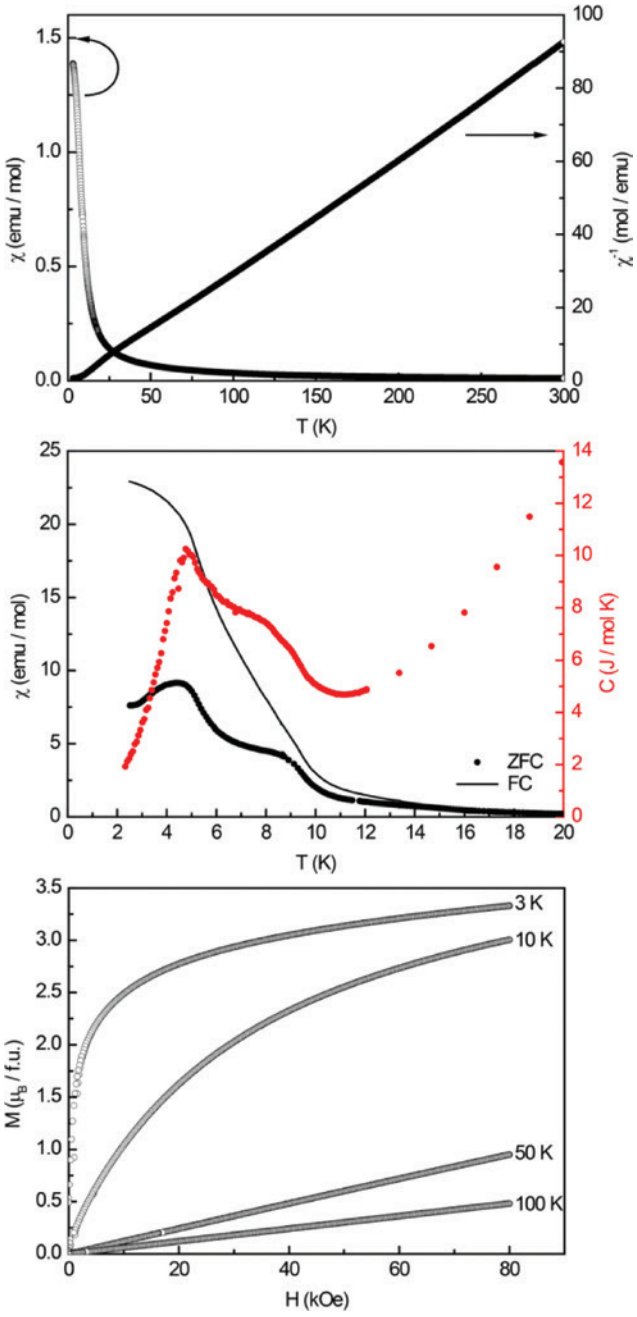

Fig. 8: Magnetic properties of Nd_2Rh_3Ga. Top: temperature dependence of the magnetic susceptibility (χ and χ^{-1} data) measured at 10 kOe. Middle: temperature dependence of the magnetic susceptibility in zero-field cooling and field cooling mode measured at 100 Oe; the heat capacity measurement is depicted in red. Bottom: magnetization isotherms at 3, 10, 50, and 100 K.

anomaly at $T = 4.8(1)$ K along with a small shoulder. The shoulder can be attributed to the impurity of the sample (although pure on the level of X-ray powder diffraction) while the main anomaly corresponds to the intrinsic magnetic transition. The ferromagnetic character of the transition is again evident from the magnetization isotherm recorded at 3 K.

The susceptibility measurements of Gd_2Rh_3Ga (Fig. 9) at 10 kOe reveal a positive Weiss constant $\theta_p = 51.7(1)$ K, suggesting ferromagnetic interactions in the paramagnetic temperature region. The ZFC/FC measurement in

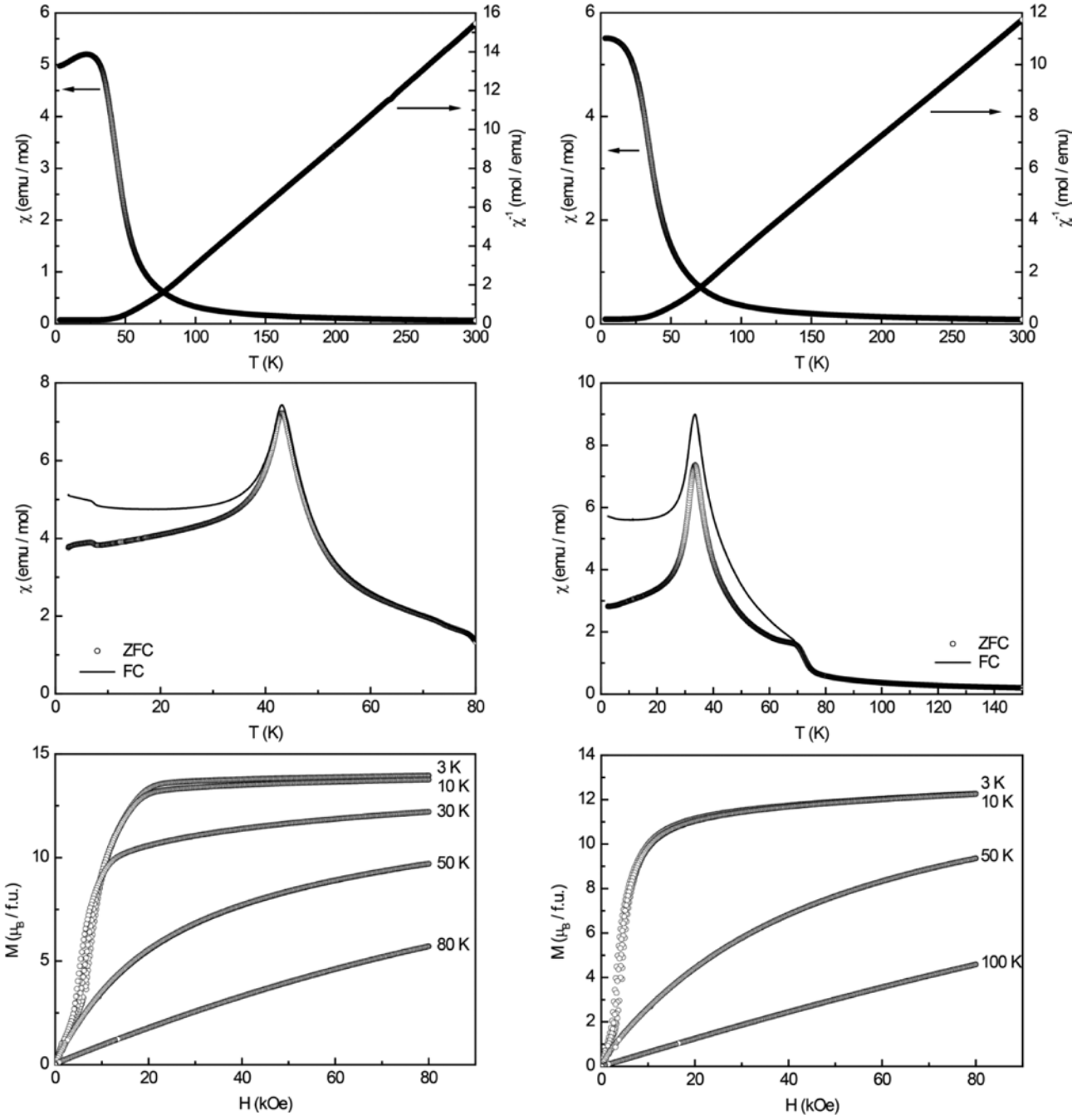

Fig. 9: Magnetic properties of Gd_2Rh_3Ga. Top: temperature dependence of the magnetic susceptibility (χ and χ^{-1} data) measured at 10 kOe. Middle: temperature dependence of the magnetic susceptibility in zero-field cooling and field cooling mode measured at 100 Oe. Bottom: magnetization isotherms at 3, 10, 30, 50, and 80 K.

Fig. 10: Magnetic properties of Tb_2Rh_3Ga. Top: temperature dependence of the magnetic susceptibility (χ and χ^{-1} data) measured at 10 kOe. Middle: temperature dependence of the magnetic susceptibility in zero-field cooling and field cooling mode measured at 100 Oe. Bottom: magnetization isotherms at 3, 10, 50, and 100 K.

contrast shows an anomaly characteristic for antiferromagnetic ordering at a Neél temperature of $T_N = 43.0(1)$ K. The antiferromagnetic character of the transition is also evident from the magnetization isotherms recorded at 3, 10 and 25 K, all showing a so called meta-magnetic step (spin-reorientation from an antiparallel to a parallel alignment). The corresponding critical field is below 10 kOe, therefore the high-field measurement suggests ferromagnetic ordering.

Similar behavior is observed for Tb_2Rh_3Ga (Fig. 10) with $\theta_P = 37.5(1)$ K. The ZFC/FC measurement shows two anomalies, one characteristic for antiferromagnetic, the

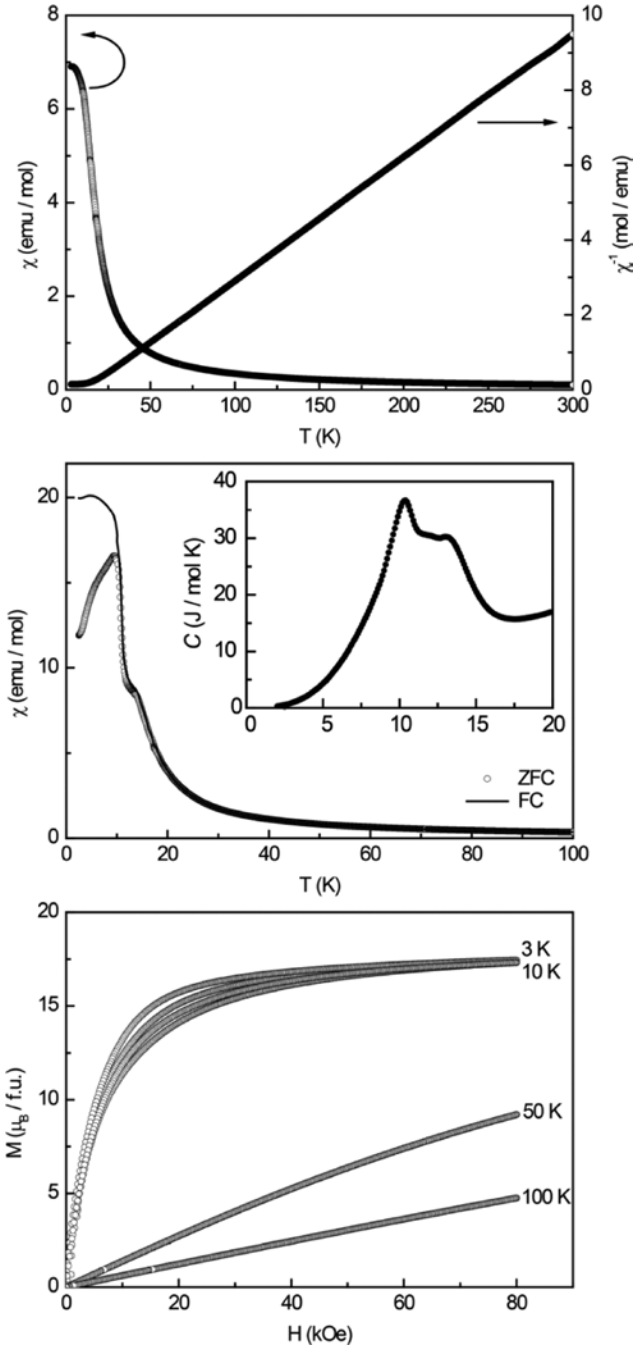

Fig. 11: Magnetic properties of Dy_2Rh_3Ga. Top: temperature dependence of the magnetic susceptibility (χ and χ^{-1} data) measured at 10 kOe. Middle: temperature dependence of the magnetic susceptibility in zero-field cooling and field cooling mode measured at 100 Oe. Bottom: magnetization isotherms at 3, 10, 50, and 100 K.

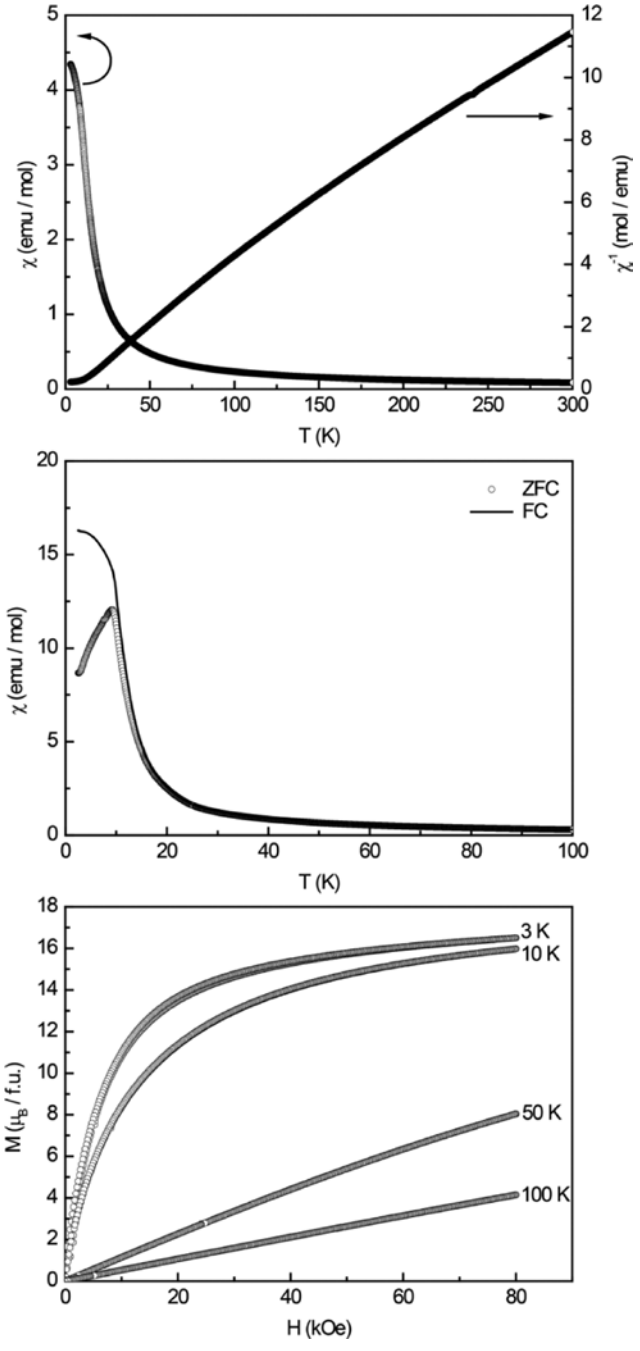

Fig. 12: Magnetic properties of Ho_2Rh_3Ga. Top: temperature dependence of the magnetic susceptibility (χ and χ^{-1} data) measured at 10 kOe. Middle: temperature dependence of the magnetic susceptibility in zero-field cooling and field cooling mode measured at 100 Oe. Bottom: magnetization isotherms at 3, 10, 50, and 100 K.

other characteristic for ferromagnetic ordering. Since the order of magnitude for the susceptibility of ferromagnetic materials is much larger compared to antiferromagnetic materials, the weak FM transition most likely originates from a tiny amount of an unknown impurity (although the sample is pure on the level of X-ray powder diffraction). For the AFM transition a Neél temperature of $T_N = 33.4(1)$ K was determined. The antiferromagnetic character of the transition is also evident from the magnetization isotherms recorded at 3 and 10 K, which show a meta-magnetic step, at a critical field below 10 kOe.

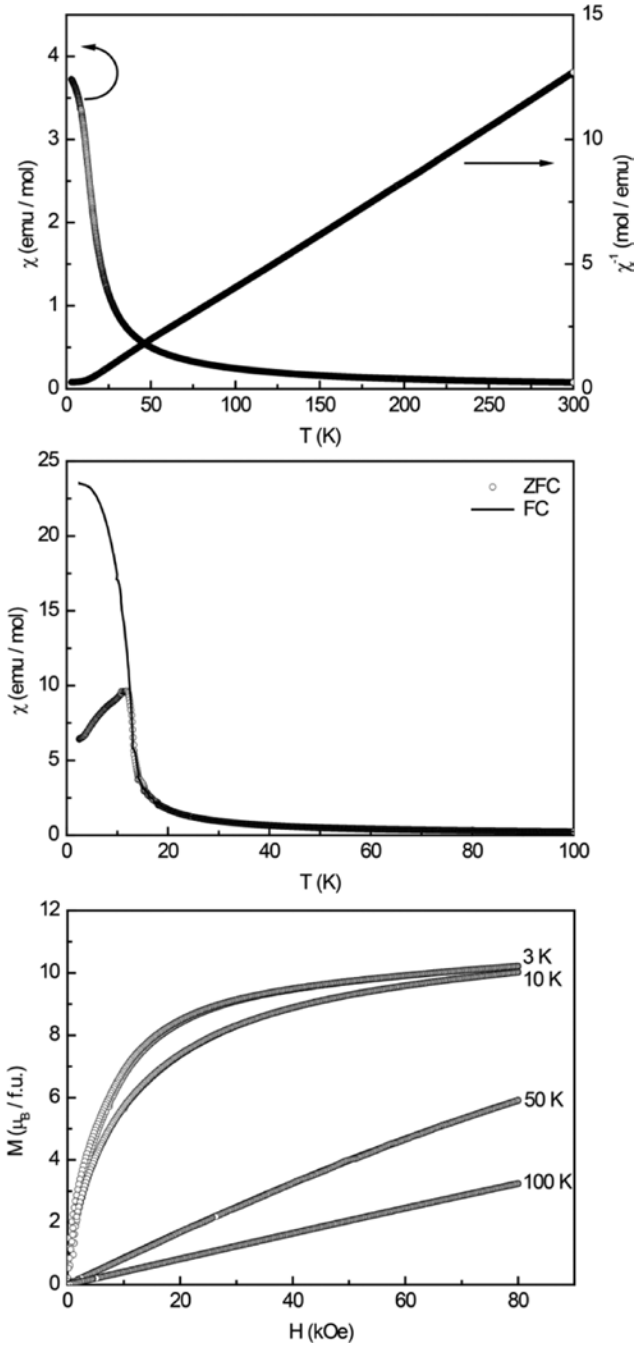

Fig. 13: Magnetic properties of Er_2Rh_3Ga. Top: temperature dependence of the magnetic susceptibility (χ and χ^{-1} data) measured at 10 kOe. Middle: temperature dependence of the magnetic susceptibility in zero-field cooling and field cooling mode measured at 100 Oe. Bottom: magnetization isotherms at 3, 10, 50, and 100 K.

The ZFC/FC measurement of Dy_2Rh_3Ga (Fig. 11) shows two anomalies with characteristics of ferromagnetic ordering at $T_{C,1} = 10.9(1)$ K and $T_{C,2} = 13.3(1)$ K. To investigate which one is intrinsic, a heat capacity measurement was conducted (Fig. 11, middle, inset). Two lambda anomalies were observed at $T = 10.4(1)$ K and $T = 13.0(1)$ K. Since the area under the signal corresponds to the amount of the respective phase present, the anomaly at $T = 10.4(1)$ K has to be the intrinsic one. The magnetization isotherms recorded at 3 and 10 K, below the ordering temperature, confirm the ferromagnetic ground state of the compound and show weak hystereses.

Ho_2Rh_3Ga (Fig. 12) and Er_2Rh_3Ga (Fig. 13) order ferromagnetically at $T_C = 10.9(1)$ and $T_C = 13.1(1)$ K, respectively. The ferromagnetic ground state of both gallides is also evident from the magnetization isotherms recorded at 3 and 10 K.

3.4 Solid state NMR spectroscopy

The ^{89}Y and ^{71}Ga solid state NMR spectra of the compound Y_2Rh_3Ga and, for comparison, the binary Laves phase YRh_2 are shown in Figs. 14 and 15. In agreement with their crystal structures, each spectrum exhibits only one single signal characterized by a very high resonance shift, which exceeds the chemical shift range of typical diamagnetic

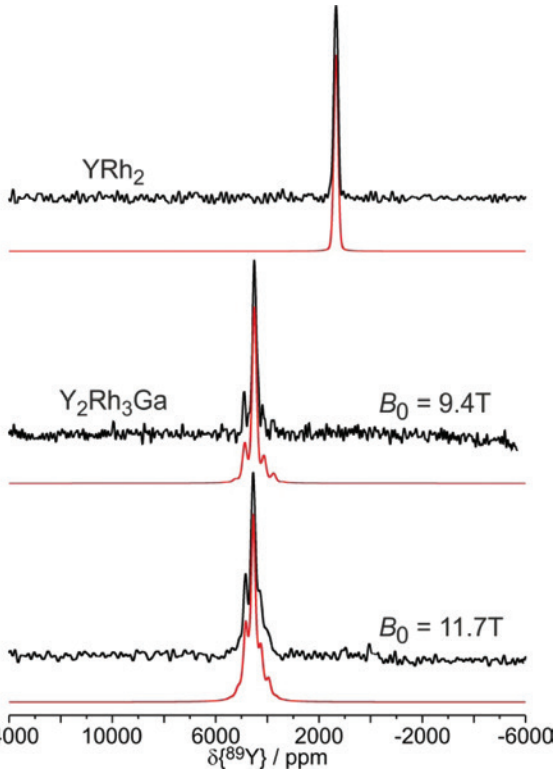

Fig. 14: Experimental and simulated (red lines) ^{89}Y MAS NMR spectra of YRh_2 (top; $B_0 = 11.7$ T; $\nu_{rot} = 4$ kHz) and Y_2Rh_3Ga (middle and bottom; $B_0 = 11.7$ T and 9.4 T; $\nu_{rot} = 7$ kHz). The signal of the ternary phase exhibits anisotropically broadened spinning sideband manifolds due to a strong Knight shift anisotropy.

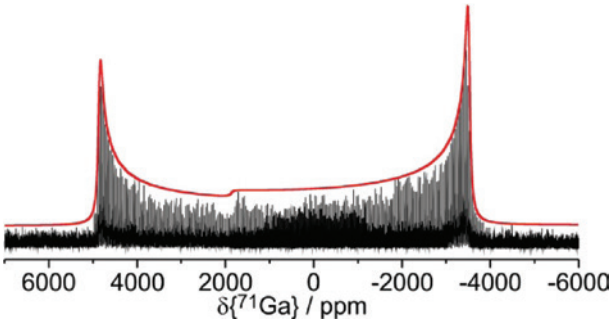

Fig. 15: Experimental ^{71}Ga NMR spectrum of Y_2Rh_3Ga with simulation (red line) recorded at an external magnetic flux density of $B_0 = 7.05$ T under static conditions.

yttrium compounds (100–400 ppm) significantly [71]. Based on the theoretical calculations discussed below we attribute the high resonance frequency to a strong Knight shift contribution originating from the interaction of the magnetic moments of the ^{89}Y and ^{71}Ga nuclei with the spin density of the conduction electrons near the Fermi edge.

The ternary Laves phase Y_2Rh_3Ga shows a significantly higher resonance frequency, suggesting a larger Knight shift contribution than observed for the binary compound YRh_2. In addition, a sizeable resonance shift anisotropy is observed, manifesting itself in a spinning sideband manifold. The difference of *s*-electron density at the Fermi-edge, also determined by total-DOS calculations (*vide infra*), suggests a partial compensation of the electron withdrawing effect of the highly electronegative Rh (EN = 2.28 [55]) atoms by the additional electron density of the Ga atoms (EN = 1.81 [55]). The observed shift anisotropy ($\Delta\sigma = -560$ ppm, $\eta_\sigma = 0$ (Table 7), observed in the field-dependent NMR spectra) is consistent with the axially symmetric local environment of the Y atoms (crystallographic 6*c* site, symmetry 3*m*).

Table 7: ^{89}Y and ^{71}Ga NMR spectroscopic parameters of Y_2Rh_3Ga and YRh_2: resonance shift δ (±1)/ppm, full width at half maximum Δ/kHz and degree of Gaussian (G) vs. Lorentzian (L) character of the signal, shift anisotropy and asymmetry parameter $\Delta\sigma$ and η_σ experimental and calculated quadrupolar coupling constant $C_{Q,\,exp}$ and $C_{Q,\,calc}$/MHz, magnetic flux density of the external field B_0/T, MAS spinning frequency ν_{rot}/kHz.

Compound	δ	Δ	G/L	Δ_σ	η_σ	$C_{Q,\,exp}$ [a]	$C_{Q,\,calc}$ [a]	B_0	ν_{rot}
Y_2Rh_3Ga									
^{89}Y	4545	4.92	0.20	−560	0	–	–	11.7	7
	4544	3.92	0.61	−560	0	–	–	9.4	7
^{71}Ga	1842	–	–	–	–	23.24	23.53	7.05	–
YRh_2									
^{89}Y	1342	4.7	0.87	–	–	–	–	11.7	4

[a] $\eta_{Q,\,calc} = \eta_{Q,\,exp} = 0$.

The lineshape of the static ^{71}Ga NMR spectrum is dominated by strong second-order quadrupolar perturbations originating from the interaction of the $I = 3/2$ nucleus with a strong electric field gradient produced by the non-cubic coordination sphere of the Ga atoms. The experimental quadrupole coupling parameters ($C_{Q,\,exp} = 23.24$ MHz, $\eta_{Q,\,exp} = 0$) are found in excellent agreement with the calculated values ($C_{Q,\,calc} = 23.53$ MHz, $\eta_{Q,\,calc} = 0$), revealing an axially symmetric electric field gradient as expected from the symmetry ($\bar{3}m$) of the Wyckoff site 3*a*. Overall, the extremely well-defined ^{71}Ga NMR spectrum characterized by a singular value of C_Q implies an essentially perfectly ordered structure and the absence of disordering and/or mixed site occupancy. The ^{71}Ga resonance shift is comparable to values found for other intermetallic gallides [72–74].

3.5 Electronic structure and NMR parameters

To understand the experimentally observed differences of the ^{89}Y NMR signal shifts, electronic structure calculations of YRh_2 and Y_2Rh_3Ga were performed. The total DOS of both compounds is presented in Fig. 16. In a first approximation, the NMR signal shift of metallic materials is frequently dominated by the s-electrons at the Fermi level (s-DOS_{EF}), since they have a nonzero probability at the nuclear site [75, 76]. This correlation was verified for the di- and tetragallides of the alkaline earth metals and $NaGa_4$ [73, 77]. Recently, the validity of this approximation has been confirmed by a careful analysis of the shift contributions in these materials [78]. Consistent with this simple correlation, Y_2Rh_3Ga possesses a significantly higher calculated s-DOS_{EF} than YRh_2 as indicated in Fig. 17.

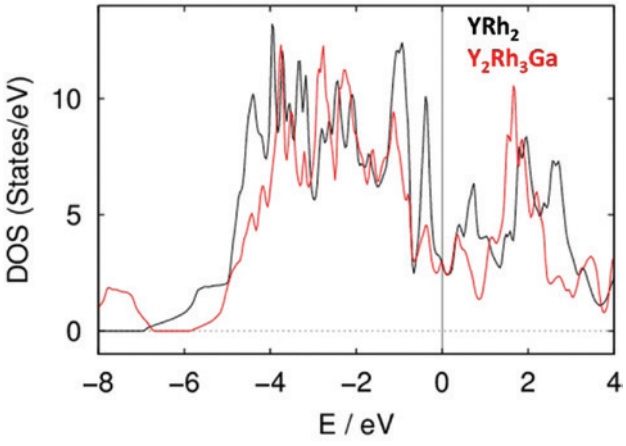

Fig. 16: Total density of states (DOS) for Y_2Rh_3Ga (red line) and YRh_2 (black line).

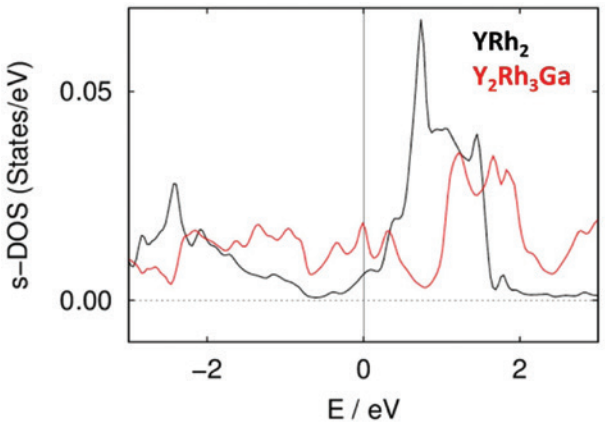

Fig. 17: s-Contributions of the angular momentum decomposed electronic density of states (*s*-DOS) for Y in YRh_2 (black) and Y_2Rh_3Ga (red).

Beside this, the calculations of the EFGs main principal axis V_{ZZ} and the asymmetry parameter η_Q of the Ga atoms are in excellent agreement with the NMR experiments (see Section 3.4 and Table 7). The highly symmetric Y_2Rh_3Ga possesses a relatively large and negative value of $V_{ZZ} = -9.092\ 10^{21}\ Vm^{-2}$. This indicates a very anisotropic prolate charge distribution of the Ga atoms compared to other Ga compounds [72–74]. The asymmetry parameter $\eta_Q = 0$ is in agreement with the experimental value and the site symmetry ($\bar{3}m$). Considering this site symmetry, V_{ZZ} has to be aligned parallel to the *c* axis of the unit cell. The charge distributions point towards the Rh triangles above and below the Ga atoms with short Rh–Ga distances. This may indicate bonding interactions of these two types of atoms.

Acknowledgments: We thank Dipl.-Ing. U. Ch. Rodewald for collection of the single crystal diffractometer data.

References

[1] F. Laves, *Theory of Alloy Phases*, Am. Soc. Met., Cleveland, **1956**.
[2] W. B. Pearson, *Acta Crystallogr. B* **1968**, *24*, 7.
[3] F. Stein, M. Palm, G. Sauthoff, *Intermetallics*, **2004**, *12*, 713.
[4] F. Stein, M. Palm, G. Sauthoff, *Intermetallics*, **2005**, *13*, 1056.
[5] K. A. Gschneidner Jr., V. K. Pecharsky, *Z. Kristallogr*. **2006**, *221*, 375.
[6] O. Eriksson, B. Johansson, M. S. S. Brooks, H. L. Skriver, *Phys. Rev. B* **1989**, *40*, 9519.
[7] K. A. Gschneidner Jr., V. K. Pecharsky, A. O. Tsokol, *Rep. Prog. Phys*. **2005**, *68*, 1479.
[8] D. Shaltiel, *J. Less-Common Met*. **1978**, *62*, 407.
[9] S. Hong, C. L. Fu, *Phys. Rev. B* **2002**, *66*, 094109.
[10] H. Kohlmann, *J. Phys. Chem. C* **2010**, *114*, 13153.
[11] E. Wu, W. Li, J. Li, *Int. J. Hydrogen Energy* **2012**, *37*, 1509.
[12] M. Y. Teslyuk, G. I. Oleksiv, *Dopov. Akad. Nauk. SSSR, Ser. B* **1965**, *10*, 1329.
[13] M. Y. Teslyuk, *Metallic Compounds with Laves Type Structure*, Nauka, Moscow, **1969**.
[14] H. Witte, *Metallwirtsch. Metallwiss. Metalltech*. **1939**, *18*, 459.
[15] E. I. Gladyshevskii, P. I. Krypyakevich, M. Y. Teslyuk, *Dopov. Akad. Nauk. SSSR*. **1952**, *85*, 81.
[16] K. Osamura, Y. Murakami, *J. Less-Common Met*. **1978**, *60*, 311.
[17] H. Arnfelt, A. Westgren, *Jernkontorets Ann*. **1935**, *118*, 185.
[18] A. Simon, W. Brämer, B. Hillenkötter, H.-J. Kullmann, *Z. Anorg. Allg. Chem*. **1976**, *419*, 253.
[19] R. Horyń, *J. Less-Common Met*. **1977**, *56*, 103.
[20] A. S. Markosyan, *Sov. Phys. Solid State* **1981**, *23*, 965.
[21] E. Gratz, *Solid State Commun*. **1983**, *48*, 825.
[22] A. C. Lawson, J. L. Smith, J. O. Willis, J. A. O'Rourke, J. Faber, R. L. Hitterman, *J. Less-Common Met*. **1985**, *107*, 243.
[23] R. Z. Levitin, A. S. Markosyan, *J. Magn. Magn. Mater*. **1990**, *84*, 247.
[24] R. Cywinski, S. H. Kilcoyne, C. A. Scott, *J. Phys.: Condens. Matter* **1991**, *3*, 6473.
[25] Y. Zhao, F. Chu, R. B. Von Dreele, Q. Zhu, *Acta Crystallogr. B* **2000**, *56*, 601.
[26] X. Yan, A. Grytsiv, P. Rogl, H. Schmidt, G. Giester, A. Saccone, X.-Q. Chen, *Intermetallics* **2009**, *17*, 336.
[27] V. Pavlyuk, G. Dmytriv, I. Tarasiuk, I. Chumak, H. Ehrenberg, *Acta Crystallogr. C* **2011**, *67*, i59.
[28] O. Osters, T. Nilges, M. Schöneich, P. Schmidt, J. Rothballer, F. Pielnhofer, R. Weihrich, *Inorg. Chem*. **2012**, *51*, 8119.
[29] Y. Mydryk, D. Paudyal, A. K. Pathak, V. K. Pecharsky, K. A. Gschneidner, Jr. *J. Mater. Chem. C* **2016**, *4*, 4521.
[30] A. E. Dwight, C. W. Kimball, *Acta Crystallogr. B* **1974**, *30*, 2791.
[31] J. Wang, Y. Feng, R. Jaramillo, J. van Wezel, P. C. Canfield, T. F. Rosenbaum, *Phys. Rev. B* **2012**, *86*, 014422.
[32] P. Villars, K. Cenzual, *Pearson's Crystal Data: Crystal Structure Database for Inorganic Compounds* (release 2015/16), ASM International®, Materials Park, Ohio (USA) **2015**.
[33] D. Noréus, L. Eriksson, L. Göthe, P.-E. Werner, *J. Less-Common Met*. **1985**, *107*, 345.
[34] K. Cenzual, B. Chabot, E. Parthé, *J. Solid State Chem*. **1987**, *70*, 229.
[35] A. Vernière, P. Lejay, P. Bordet, J. Chenavas, J. P. Brison, P. Haen, J. X. Boucherle, *J. Alloys Compd*. **1994**, *209*, 251.
[36] A. Lipatov, A. Gribanov, A. Grytsiv, S. Safronov, P. Rogl, J. Rousnyak, Y. Seropegin, G. Giester, *J. Solid State Chem*. **2010**, *183*, 829.
[37] D. Kaczorowski, A. Lipatov, A. Gribanov, Yu. Seropegin, *J. Alloys Compd*. **2011**, *509*, 6518.
[38] I. Doverbratt, S. Ponou, S. Lidin, *J. Solid State Chem*. **2013**, *197*, 312.
[39] A. V. Morozkin, *J. Alloys Compd*. **2004**, *385*, L1.
[40] V. Keimes, A. Mewis, *Z. Naturforsch*. **1992**, *47b*, 1351.
[41] R. Pöttgen, A. Lang, R.-D. Hoffmann, B. Künnen, G. Kotzyba, R. Müllmann, B. D. Mosel, C. Rosenhahn, *Z. Kristallogr*. **1999**, *214*, 143.
[42] K. Yvon, W. Jeitschko, E. Parthé, *J. Appl. Crystallogr*. **1977**, *10*, 73.
[43] L. A. O'Dell, R. W. Schurko, *Chem. Phys. Lett*. **2008**, *464*, 97.
[44] Bruker Corp., Topspin (Version 2.1), Karlsruhe, Germany, **2008**.

[45] D. Massiot, F. Fayon, M. Capron, I. King, S. Le Calvé, B. Alonso, J.-O. Durand, B. Bujoli, Z. Gan, G. Hoatson, *Magn. Reson. Chem*. **2002**, *40*, 70.
[46] H. M. Petrilli, P. E. Blöchl, P. Blaha, K. Schwarz, *Phys. Rev.* B **1998**, *57*, 14690.
[47] G. Kresse, J. Furthmüller, *Phys. Rev. B*, **1996**, *54*, 11169.
[48] P. Blaha, K. Schwarz, G. K. H. Madsen, D. Kvasnicka, J. Luitz, WIEN2k, Vienna University of Technology, Vienna, Austria, **2001**.
[49] J. P. Perdew, K. Burke, M. Ernzerhof, *Phys. Rev. Lett.* **1996**, *77*, 3865.
[50] V. Petříček, M. Dušek, L. Palatinus, JANA2006, The Crystallographic Computing System, Institute of Physics, Academy of Sciences of the Czech Republic, Prague (Czech Republic) **2006**.
[51] V. Petříček, M. Dušek, L. Palatinus, *Z. Kristallogr.* **2014**, *229*, 345.
[52] V. B. Compton, B. T. Matthias, *Acta Crystallogr*. **1959**, *12*, 651.
[53] F. Hulliger, *J. Alloys Compd*. **1996**, *239*, 131.
[54] N. C. Baenziger, J. L. Moriarty Jr., *Acta Crystallogr*. **1961**, *14*, 948.
[55] J. Emsley, *The Elements*, Oxford University Press, Oxford **1999**.
[56] B. Chevalier, B. Heying, U. Ch. Rodewald, C. Peter Sebastian, E. Bauer, R. Pöttgen, *Chem. Mater*. **2007**, *19*, 3052.
[57] O. Sichevych, W. Schnelle, Yu. Prots, U. Burkhardt, Yu. Grin, *Z. Naturforsch*. **2006**, *61b*, 904.
[58] H. H. Hill, in *Plutonium and Other Actinides, Nuclear Materials Series, AIME*, (Ed.: W. N. Mines), **1970**, *17*, 2.
[59] H. Bärnighausen, *Commun. Math. Chem*. **1980**, *9*, 139.
[60] U. Müller, *Z. Anorg. Allg. Chem*. **2004**, *630*, 1519.
[61] U. Müller, *Symmetriebeziehungen zwischen verwandten Kristallstrukturen*, Vieweg, Teubner Verlag, Wiesbaden, **2012**.
[62] R. L. Johnston, R. Hoffmann, *Z. Anorg. Allg. Chem*. **1992**, *616*, 105.
[63] L. L. Hirst, *Phys. Kondens. Materie* **1970**, *11*, 255.
[64] B. C. Sales, D. K. Wohlleben, *Phys. Rev. Lett.* **1975**, *35*, 1240.
[65] U. B. Paramanik, Anupam, U. Burkhardt, R. Prasad, C. Geibel, Z. Hossain, *J. Alloys Compd*. **2013**, *580*, 435.
[66] D. Kaczorowski, A. P. Pikul, U. Burkhardt, M. Schmidt, A. Ślebarski, A. Szajek, M. Werwiński, Y. Grin, *J. Phys.: Condens. Matter* **2010**, *22*, 215601.
[67] O. Niehaus, U. C. Rodewald, P. M. Abdala, R. S. Touzani, B. P. T. Fokwa, O. Janka, *Inorg. Chem.* **2014**, *53*, 2471.
[68] O. Niehaus, P. M. Abdala, R. Pöttgen, *Z. Naturforsch*. **2015**, *70b*, 253.
[69] H. Sugawara, T. Yamazaki, J. Itoh, M. Takashita, T. Ebihara, N. Kimura, P. Svoboda, R. Settai, Y. Ōnuki, H. Aoki, S. Uji, *Physica B* **1994**, *199 & 200*, 570.
[70] T. Mihalisin, A. Harrus, S. Raaen, R. D. Parks, *J. Appl. Phys*. **1984**, *55*, 1966.
[71] J. Mason, *Multinuclear NMR*, Kluwer Academic/Plenum Publishers, Buckinghamshire, **1987**.
[72] F. Haarmann, K. Koch, D. Grüner, W. Schnelle, O. Pecher, R. Cardoso-Gil, H. Borrmann, H. Rosner, Yu. Grin, *Chem. Eur. J*. **2009**, *15*, 1673.
[73] F. Haarmann, K. Koch, P. Jeglič, O. Pecher, H. Rosner, Yu. Grin, *Chem. Eur. J*. **2011**, *17*, 7560.
[74] L. Vasylechko, U. Burkhardt, W. Schnelle, H. Borrmann, F. Haarmann, A. Senyshyn, D. Trots, K. Hiebl, Yu. Grin, *Solid State Sci*. **2012**, *14*, 746.
[75] A. Abragam, *Principles of Nuclear Magnetism*, Oxford University Press, Oxford, New York, **1961**.
[76] C. P. Slichter, *Principles of Magnetic Resonance*, 3rd ed., Springer-Verlag, Berlin, Heidelberg, New York, **1990**.
[77] F. Haarmann, *Quadrupolar NMR of Intermetallic Compounds*, in *Enzyclopedia of Magnetic Resonance*, (Eds.: R. K. Harris, R. E. Wasylishen), John Wiley & Sons, Ltd, Chichester, **2011**.
[78] R. Laskowski, K. H. Khoo, F. Haarmann, P. Blaha, *J. Phys. Chem. C* **2017**, *121*, 753.